Insight into the collective vibrational modes driving ultralow thermal conductivity of perovskite solar cells

Sheng-Ying Yue, Xiaoliang Zhang, Guangzhao Qin, Jiayue Yang, and Ming Hu

Phys. Rev. B **94**, 115427 — Published 20 September 2016

DOI: 10.1103/PhysRevB.94.115427

Insight into the Collective Vibrational Modes Driving Ultra-low Thermal Conductivity of Perovskite Solar Cells

Sheng-Ying Yue †,[1] Xiaoliang Zhang †,[2] Guangzhao Qin,[2] Jiayue Yang,[2] and Ming Hu[1,2,*]

[1] *Aachen Institute for Advanced Study in Computational Engineering Science (AICES), RWTH Aachen University, 52062 Aachen, Germany*

[2] *Institute of Mineral Engineering, Division of Materials Science and Engineering, Faculty of Georesources and Materials Engineering, RWTH Aachen University, 52064 Aachen, Germany*

The past few years have witnessed a rapid evolution of hybrid organic-inorganic perovskite solar cells as an unprecedented photovoltaic technology with both relatively low cost and high power conversion. The fascinating physical and chemical properties of perovskites are benefited from their unique crystal structures represented by the general chemical formula AMX_3, where the A cations occupy the hollows formed by the MX_3 octahedra and thus balance the charge of the entire network. Despite a vast amount of theoretical and experimental investigations have been dedicated to the structural stability, electrical, and optical properties of hybrid halide perovskite materials in relation to their applications in solar cells, the thermal transport property, another critical parameter to the design and optimization of relevant solar cell modules, receives less attention. In this paper, we evaluate the lattice thermal conductivity of a representative methylammonium lead triiodide perovskite ($CH_3NH_3PbI_3$) with direct non-equilibrium *ab initio* molecular dynamics simulation. Resorting to full first-principle calculations, we illustrate the details of the mysterious vibration of the methylammonium cluster ($CH_3NH_3^+$) and present an unambiguous picture of how the organic cluster interacting with the inorganic cage and how the collective motions of the organic cluster drags the thermal transport, which provide fundamental understanding of the ultra-low thermal conductivity of $CH_3NH_3PbI_3$. We also reveal the strongly localized phonons associated with the internal motions of the $CH_3NH_3^+$ cluster, which contribute little to the total thermal conductivity. The importance of the $CH_3NH_3^+$ cluster to the structural instability is also discussed in terms of the unconventional dispersion curves by freezing the partial freedoms of the organic cluster. These results provide more quantitative description of organic-inorganic interaction and coupling dynamics from accurate first-principles calculations, which are expected to underpin the development of emerging photovoltaic devices.

I. INTRODUCTION

Hybrid organic-inorganic solar cells based on methylammonium lead triiodide perovskite structures ($CH_3NH_3PbI_3$, abbreviated as MAPI) have gained substantial attention due to their unrivalled potential for large-scale renewable energy production and greenhouse gas emissions reduction, due to their cheap price, high absorption coefficient, highly efficient solar energy conversion with a short energy payback time and easy process solution [1–7]. Among the unique physical and chemical properties of perovskite structures, thermal transport property is an important parameter that is critical to the design of device level application of the perovskite structure based solar cells. From thermal management point of view, study of intrinsic thermal conductivity of perovskite structures will facilitate optimizing the working performance of the solar cell at finite temperature and underpin the relevant development of emerging photovoltaic devices. Previous studies have established general knowledge that, MAPI is characterized by an intrinsic ultra-low lattice thermal conductivity (κ) of $\sim$ 0.5 W/(mK) at room temperature [8–10], which is far lower than that for pure inorganic perovskites. Motivated by this, recent research also demonstrates the potential of MAPI as a candidate of waste heat recovery (thermoelectrics) because of the high Seebeck coefficient [11] and the ultra-low κ.

However, the physical mechanism underlying the ultra-low κ of these fascinating materials remains sparse. Recently, several works attempted to clarify the interactions between the methylammonium cluster ($CH_3NH_3^+$, abbreviated as MA^+) and the inorganic cage [9, 12]. From the aspect of degree of freedom, T. Hata et al. compared and analysed the effect of MA^+ in heat transfer through classical molecular dynamics (MD) simulations [9]. Despite some mechanism proposed, the accuracy of the results is sometimes questionable due to the empirical potential used. A. Leguy et al. used quasielastic neutron scattering method to measure the motions of MA^+ in MAPI directly [12]. Although the IR and Raman spectra present that the vibrational density of states (VDOS) of the inorganic cage mainly overlaps with rotation of MA^+ [13–15], which implies that the interaction between the rotational motions of MA^+ and the lattice phonon waves is the dominant mechanism for the attenuation of heat transfer [8], the physical picture of the phonon transport in MAPI still remains unclear. In particular, how the motions of MA^+ couple with the inorganic lattice vibra-

†These authors contribute equally to this work.
*Electronic address: hum@ghi.rwth-aachen.de

tions? Which motions (specifically with how much vibrational frequency) dominate the suppression of κ of the hybrid system, and which motions are useless in terms of heat transfer? The answers to such questions are not only important to deeply understand the mechanism of thermal transport, but also significant to the advanced studies and development of broad hybrid organic-inorganic systems.

In this paper, for the first time we perform direct non-equilibrium *ab initio* molecular dynamics (NEAIMD) simulation to evaluate the κ of MAPI with different structural phases. Our full first-principles calculation manifests itself in that the simulations are conducted without any artificial input parameters. We first investigate the role of the organic cluster in the structural stability by examining the effective phonon dispersions of the inorganic cage through freezing the partial motions of the organic cluster. We observe that the frequencies in MAPI are split into three isolated islands, which play a significant role in the phonon transport property and show direct evidence for the coupling of motions between the organic cluster and the inorganic cage. We also run the equilibrium ab initio molecular dynamics (EAIMD) combining with the spectral energy density (SED) technique to clarify the partial VDOS and phonon lifetime, through which we provide the solid evidence that the middle and high frequency islands do not have actual contribution to the overall thermal transport, despite of their moderate phonon lifetime. It should be noted that some previous papers have studied the thermodynamic properties of MAPI, e.g. in the research of F. Brivio et al. the phonon dispersions and vibrational modes have been studied in detail [15]. However, the normal modes in the F. Brivio et al.'s work are still calculated within the traditional harmonic approximation [15], which can only present the eigenvectors of the vibrational modes, but cannot reflect the real velocities and displacements of the vibrational modes at finite temperature. To further get the insight into the thermodynamic properties of MAPI, we develop the aforementioned method to observe the specific phonon modes of MAPI by performing normal mode analysis based on direct EAIMD simulation and visualization of all motions of phonon modes in the real time and space. In the meantime, we extract data from EAIMD simulation and quantitatively characterize the the anharmonicity of different phonon modes induced by the collective motions of the MA^+ cluster. These results provide coherent understanding of the relationship between the intrinsic ultra-low κ and the distinct organic-inorganic interactions, and the unique cage-like structure of $CH_3NH_3PbI_3$.

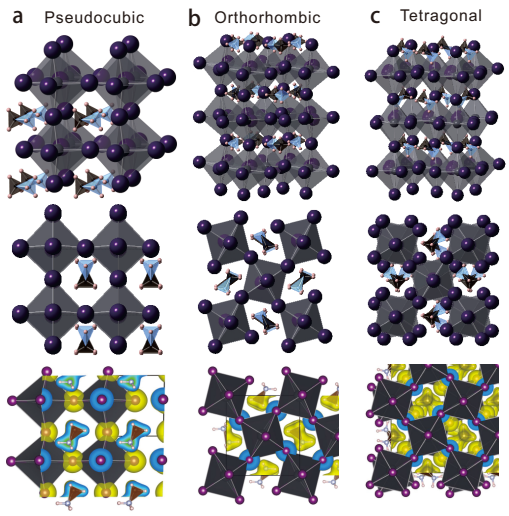

FIG. 1: The side-view (top panel), top-view (middle panel) and the spatial charge density (bottom panel) of (a) pseudocubic, (b) orthorhombic and (c) tetragonal phase of methylammonium lead triiodide perovskite structures ($CH_3NH_3PbI_3$, MAPI).

II. METHODS

A. Setup of NEAIMD simulation

The structures of the three different phases studied in this work, namely pseudocubic, orthorhombic and tetragonal phase $CH_3NH_3PbI_3$, are illustrated in the top and middle panels of Fig. 1. We evaluate the κ of the pseudocubic and tetragonal MAPI through NEAIMD method. The size of the simulation models ranges from $2 \times 2 \times 8$ unit cells (348 atoms in total) to $2 \times 2 \times 12$ unit cells (540 atoms) for pseudocubic and from $1 \times 1 \times 6$ unit cells (144 atoms) to $1 \times 1 \times 12$ unit cells (288 atoms) for tetragonal phase. All NEAIMD simulations [16, 17] are performed by the modified Vienna Ab initio Simulation Package (VASP) [18, 19]. The energy cutoff of plane wave is taken as 400 eV. For the parameter of the partial occupancies we adopt the Gaussian smearing with the width of the smearing of 0.01 eV. The timestep of NEAIMD simulation is 1 fs. At both ends of the models, one layer atoms are fixed and a vacuum layer with thickness of $\sim$ 6.5 Å is set, which is equivalent to the fixed boundary condition used in the heat flux direction (longitudinal direction). Periodical boundaries conditions are used in the other two dimensions, i.e. in the lateral directions. The atomic heat flux (J) is realized by using the Müller-Plathe algorithm [20], in which the kinetic energies of the atoms in the heat source and heat sink are exchanged every 50 fs (Fig. 2(a, b)). The NEAIMD simulation time (typically $\sim$ 10 ps) is sufficiently longer than the rotational relaxation time and correlation time of MA^+ (5.37 ps and 0.46 ps [21], re-

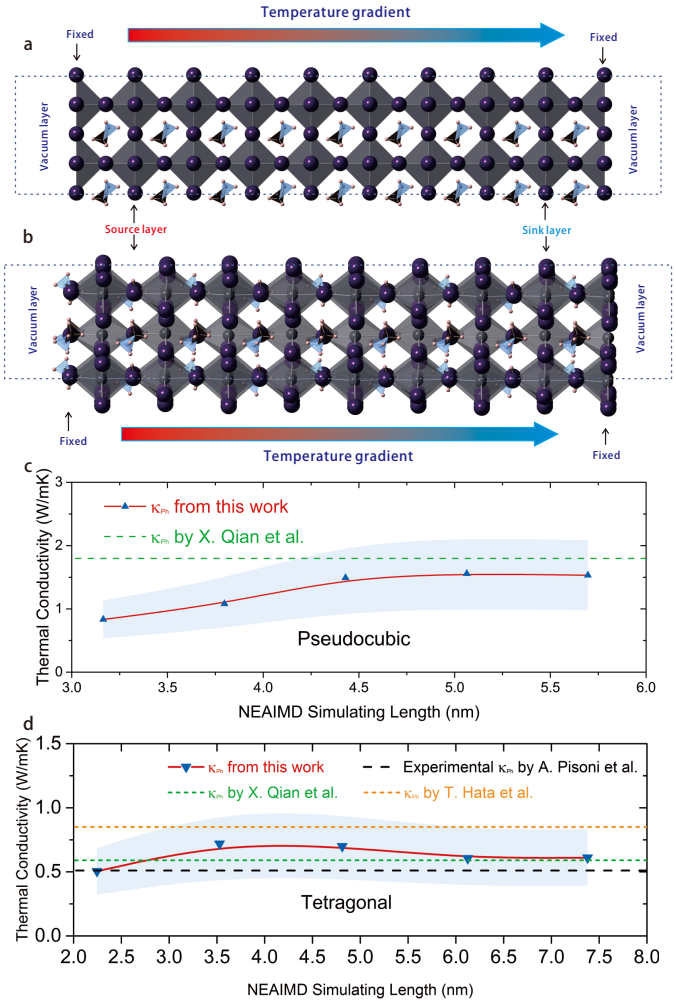

FIG. 2: NEAIMD simulation models of (a) pseudocubic and (b) tetragonal phase MAPI. (c) and (d) are the corresponding length dependent thermal conductivity. The shaded area indicate the error bar of the NEAIMD simulation. The green and yellow dotted lines are thermal conductivity results from previous theoretical calculations [9, 10], and the black dashed line denotes experimental data [8].

spectively). It is worth pointing out that, we perform EAIMD simulation with NVE (constant particle and volume without thermostat) ensemble before NEAIMD simulation. We have carefully checked that the initial temperature of the EAIMD simulation is well chosen, and both the temperature and potential energy of the system fluctuate randomly around their respective constant value (the average temperature is the target temperature as expected) at the end of EAIMD simulation ($\sim$ 5 ps), which means the system has already reached equilibrium state. Then a stable temperature gradient (∇T) along the heat flow direction in MAPI can be established during the NEAIMD simulation. A representative case with accumulated exchange atomic energy with simulation time and the corresponding average temperature profile can be found in Supplemental Material. Finally, we can calculate κ based on Fourier's law: $J = -\kappa\ \nabla T$. We also provide a supporting movie of NEAIMD simulation to show how the atoms move under the temperature gradient. It is well known that, the size effect is inevitable in calculating thermal conductivity using non-equilibrium molecular dynamics simulation. To avoid the size effect of NEAIMD, we performed different lengths of two MAPI structures (Fig. 2(c, d)) to obtain the effective bulk κ. Each data point reported here refers to the average of five independent runs. The temperature of NEAIMD simulation for the pseudocubic and tetragonal phase is $\sim$ 320 K and $\sim$ 300 K, respectively.

B. Phonon dispersion calculation

For rather long time, the material instability of MAPI remains a major obstacle to its broad application, which

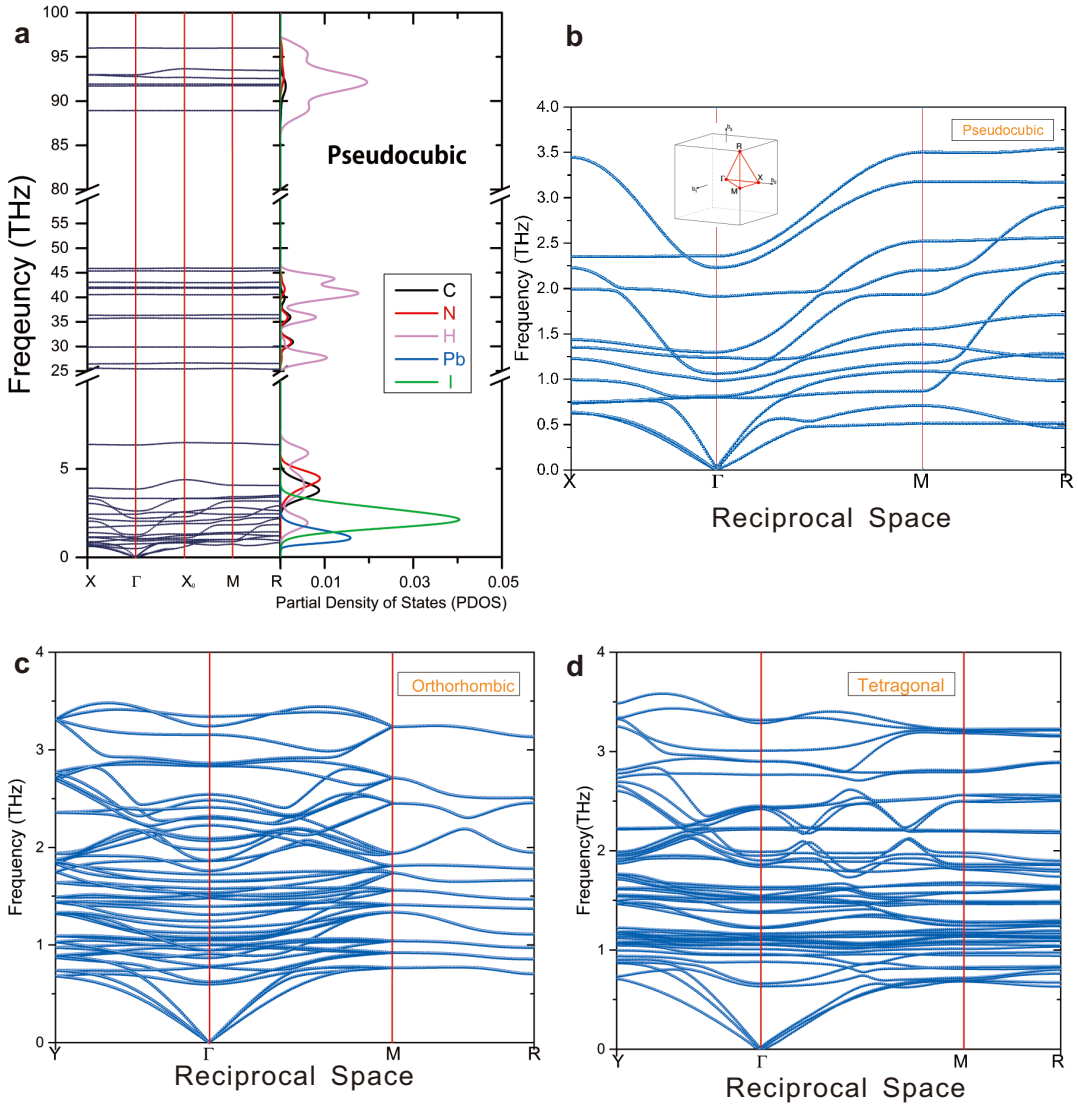

FIG. 3: (a) The full phonon dispersion curves (left panel) of pseudocubic phase MAPI and the corresponding partial phonon density of states (right panel), where the low, middle and high frequency islands are clearly identified. (b-d) The low frequency phonon dispersion curves of only inorganic cages for the pseudocubic, orthorhombic and tetragonal phase, respectively, by freezing the motions of the MA^+ cluster (see text for details).

is usually judged by the real vibrational frequencies in the phonon dispersion curves. In the research work of Motta et al. [22], the phonon dispersion curves are presented with imaginary frequencies in the first Brillouin zone. They attribute these unstable modes to that the system spontaneously tends to its zero-temperature ground state [22]. However, this explanation is not convincing enough. Based on the Motta et al.'s explanation [22], the two phases (tetragonal and pseudocubic) except the zero-temperature ground state (orthorhombic) should have unstable (imaginary) modes. However, with density functional theory (DFT) calculations, Brivio et al. [15] stated that no imaginary (negative) modes are found in the tetragonal phases of MAPI, which conflicts with the Motta et al.'s explanation [22]. Here, with finite displacement difference method implemented in the Phonopy package [23], we calculate the phonon dispersion curves based on density functional theory of VASP. The Perdew-Burke-Ernzerhof parameterization of the generalized gradient approximation (GGA) [24] is used for the exchange-correlated functional, and the projector-augmented wave (PAW) [25, 26] method is applied to model the core electrons (for Pb the 5d orbitals are included). The energy cutoff of plane wave is set as 700 eV. For the parameter of the partial occupancies we adopt the Gaussian smearing and the width of the smearing is 0.01 eV. The van der Waals (vdW) interactions are also considered as non-bonded terms [27]. When we calculate the low frequency dispersion curves, we treat the MA^+ cluster as a whole rigid object which means we freeze the inner freedoms

belonging to the MA^+ cluster. In other words, we only consider the freedom of Pb-I cages and the freedoms of MA^+ cluster as a whole. For orthorhombic and tetragonal phases the unit cell contains 48 atoms, and the pseudocubic phase has 12 atoms in the unit cell. Here we take $2 \times 2 \times 2$ supercell for all three phases and use $6 \times 6 \times 6$ Monkhorst-Pack grids for $k-$point sampling. With this method we present the phonon dispersion curves of three phases in Fig. 3(b-d).

We also calculated the full dispersion curves of the pseudocubic phase with traditional finite displacement method, i.e. solving the dynamical matrix for all atoms in the unit cell, and modified the low frequency branches with that obtained by the above method of freezing the partial freedoms of the MA^+ cluster to avoid the imaginary frequency of phonon branches. The full dispersion curves are shown in the left panel of Fig. 3(a). With the full dispersion curves the phonon group velocities ($\vec{v}_g$) can be obtained by $\vec{v}_g = \frac{d\,\omega}{d\,\vec{k}}$, where ω is the phonon frequency and $\vec{k}$ is the momentum vector of phonons in $k-$space. Simultaneously, we obtain the partial density of states (PDOS) with Phonopy package [23] (right panel of Fig. 3(a)).

C. EAIMD simulation, SED and normal mode analysis

To explicitly study the interactions between MA^+ and the inorganic lattice, we performed the EAIMD simulations for the pseudocubic phase. The energy cutoff of plane wave we take is 400 eV. For the parameter of the partial occupancies we adopt the Gaussian smearing and the width of the smearing is 0.01 eV. The supercell size is $2 \times 2 \times 2$ unit cells and the simulation temperature is around 300 K. The total NVE simulation time is about 16 ps. With the atomic velocity recorded from NVE simulation, the VDOS can be calculated by performing the Fourier transform of the auto-correlation function of atomic velocity [28, 29]

$$\mathrm{VDOS}(f) \;=\; \int \gamma(t)\exp(-2\pi i f t)dt,$$

where $\gamma(t)$ is defined as $\gamma(t) = \frac{\langle \Sigma_i v_i(0)\cdot v_i(t)\rangle}{\langle \Sigma_i v_i(0)\cdot v_i(0)\rangle}$, and $v_i(t)$ represents the velocity of the i^{th} atom at time t. To see the interaction between MA^+ and PbI_3^-, we also perform EAIMD simulation of the inorganic cages without MA^+ for $\sim$ 17 ps, where the positive charge background is used, and calculate the corresponding VDOS.

Based on the EAIMD simulations, we further use the SED technique [30–32] to extract the phonon lifetime of each specific mode. The SED is calculated by [31]

$$\Phi(\vec{k},\nu,f) \;=\; |\int \dot{\mathrm{Q}}(\vec{k},\nu,t)\exp(-2\pi i f t)dt|^2,$$

where f is frequency and the phonon normal mode can be obtained as $\dot{\mathrm{Q}}(\vec{k},\nu,t) = \Sigma_{jl}\sqrt{\frac{m_j}{N}}\vec{v}_{jl}(t)\cdot \vec{e}_j^*(\vec{k},\nu)\exp(-2\pi i\vec{k}\cdot\vec{r}_l)$. Here, m_j is the mass of the j^{th} basis atom, N is the number of unit cells, $\vec{v}_{jl}(t)$ is the velocity of the j^{th} basis atom in the l^{th} unit cell at time t, $\vec{e}_j^*(\vec{k},\nu)$ is the complex conjugate of the eigenvector of the phonon mode $\vec{e}(\vec{k},\nu)$ of the j^{th} basis atom, $\vec{k}$ is the wave vector and ν is the phonon index [33]. We run five independent EAIMD simulations to take the ensemble average in calculating SED. After that, the phonon lifetime of each mode can be obtained by fitting the SED peak using the Lorentzian function [30]

$$\Phi(\vec{k},\nu,f) \;=\; \frac{I}{1+\left[\frac{2\pi(f-f_0)}{\Gamma}\right]^2},$$

where I is the peak magnitude, f_0 is the frequency at the peak center, Γ is the half-width at half-maximum. Finally, the phonon lifetime (τ) can be obtained by $\tau = \frac{1}{2\Gamma}$.

To analyse the detailed dynamic motion of atoms associated with a specific phonon mode, we obtain the mode-dependent velocity field by performing the inverse Fourier transform to the phonon normal modes [33]

$$\vec{v}_{jl}(\vec{k},\nu,t) \;=\; \dot{\mathrm{Q}}(\vec{k},\nu,t)\vec{e}_j(\vec{k},\nu)\exp(2\pi i\vec{k}\cdot\vec{r}_l).$$

Then the mode-dependent atomic trajectory can be obtained according to

$$\vec{r}_{jl}(\vec{k},\nu,t+\Delta t) = \vec{r}_{jl}(\vec{k},\nu,t) + \vec{v}_{jl}(\vec{k},\nu,t)\Delta t,$$

where $\vec{r}_{jl}(\vec{k},\nu,t)$ is the mode-dependent atomic position of the j^{th} basis atom in the l^{th} unit cell at time t and Δt is the timestep.

III. RESULTS AND DISCUSSION

A. Thermal conductivity from NEAIMD simulation

After the structure is optimized, we calculate the spatial electronic charge density of three phases, also shown in the bottom panel of Fig. 1. We can see that clearly, there are enough space in the inorganic cages to allow the MA^+ molecules to move. Such space provides the opportunity of multiple motions of MA^+ at finite temperature, as we will see later.

With NEAIMD method, we obtain the converged κ with respect to simulation length (Fig. 2(c, d)). Since the orthorhombic phase belongs to low temperature range, which is beyond the temperature range usually used for photovoltaic applications, we only simulate the pseudocubic and tetragonal phases here. In Fig. 2(c), the converged κ of the pseudocubic phase from our NEAIMD simulation is 1.56 W/(mK) around 320 K. This value is very close to the previous result from empirical potential method (classical MD) by X. Qian et al. [10], which is 1.80 W/(mK) at 329 K. From the behaviour

of the length dependent κ, we estimate that the phonon mean free path (MFP) of the pseudocubic phase MAPI is $\sim$ 4.5 nm, based on the fact that when $L \sim$ MFP the thermal transport goes into diffusive regime, corresponding to converged κ vs. L. In Fig. 2(d), we present our NEAIMD results of κ for the tetragonal phase as compared with previous results from classical MD simulations ($\sim$ 0.59 W/(mK) by X. Qian et al. [10] and $\sim$ 0.85 W/(mK) by T. Hata et al. [9]) and experimental measurements [8] ($\sim$ 0.51 W/(mK)). Our converged κ value of MAPI is 0.61 W/(mK) around 300 K, which agrees very well with experimental value. We can also infer that the MFP of the tetragonal phase is only $\sim$ 3.0 nm. The very short MFP of both pseudocubic and tetragonal phases is a direct evidence of the drastic phonon scattering in such hybrid organic-inorganic structures. In addition, combining X. Qian et al.'s results [10] and our work, a sharp phase jump is expected at the transition temperature.

B. Analysis of phonon dispersion, group velocity and lifetime

By freezing the motions of the MA^+ cluster we successfully eliminate the unstable phonon branches, i.e. those with imaginary frequencies, in the phonon dispersion curves of three structures, as shown in Fig. 3(b-d). In addition, we have checked that, for the whole Brillouin zone there are no imaginary modes when this approach is adopted. It means that the thermodynamic stability of MAPI completely originates from the motions of the MA^+ cluster, and the reason behind the unstable imaginary modes is solely because of the interaction between the MA^+ inner freedoms and the Pb-I cages. We also note that without MA^+ the PbI_3^- cage cannot be thermodynamically stable alone. To analyse the phonon transport behaviour and understand the contribution of each phonon mode to κ, we present the full phonon dispersion curves and the PDOS of pseudocubic MAPI in Fig. 3(a). We can see very clearly that, the phonon frequencies available in pseudocubic MAPI can be separated into three islands. The lowest frequency island is below $\sim$ 7 THz, the middle island ranges from 25 THz to 45 THz, and the highest island is beyond 89 THz. Among the islands, there exist huge energy gaps, from which we expect reduced phonon scattering among the islands. However, one cannot intuitively speculate high thermal conductivity, as we will see more clearly below.

From the PDOS in Fig. 3(a), we learn that the PDOS of both Pb and I ions are located in the lowest frequency island, which is consistent with our phonon dispersion curves shown in Fig. 3(b). This finding is also similar to the previous study that the Pb-I modes from the low energy island contribute to the ionic screening and the higher energy modes do not [34]. It is worth noting that, the lowest island also contains the PDOS of C, N, and H atoms, which are thought to come from the MA^+ cluster. Actually, these phonons correspond to the motion of MA^+ as a whole unit, such as the translational and rotational movement inside the inorganic cage. Because the MA^+ unit has positive charge and the inorganic cage has negative charge, these low frequency modes of MA^+ dominate the interactions between the organic and inorganic parts. These interactions can be observed straightforwardly from the phonon modes presented in the supporting movies (Vibrational modes $01-24$). The middle island only contains the PDOS of C, N, and H atoms. Theses phonon modes in the middle island mostly correspond to the relative movement between the $-CH_3$ group and the $-NH_3$ group composing the MA^+ cluster, such as the shearing and stretching modes of C$-$N bond (supporting movies: Vibrational modes $25-36$). Since these modes belong to the inner motions of the MA^+ and the corresponding phonon dispersion curves are almost flat in the first Brillouin zone (Fig. 3(a)), they possess almost zero phonon group velocities, as seen in Fig. 4(a). On the other hand, because of the enough space in the PbI_3^- cages as shown in Fig. 1(a), the inorganic cages almost isolate the organic parts in a closed space, which induces that these internal modes can hardly scatter with the motions from outside and thus have relatively not very small lifetimes (Fig.4(b)). As we mentioned earlier, there exist huge energy gaps among the three islands in the PDOS and such gaps could prevent the phonon scattering among the islands. Actually, the huge energy gap disables the phonon scattering between the internal motions of the organic cluster (middle frequency island) and the lattice vibrations of the inorganic cages (low frequency island). The two physical pictures demonstrated here are consistent with each other. As for the highest island, the PDOS is dominated by the H atoms. The phonon modes in this island mainly correspond to the movements of the C$-$H and N$-$H bonds, such as bond swing and stretching (also can be seen in the supporting movies: Vibrational modes $25-36$). Same as the middle frequency island, the phonon group velocities of the highest island are also nearly zero but the phonon lifetimes are not zero (Fig. 4).

From the phonon Boltzmann transport equation (BTE) with single relaxation time approximation, we know that $\kappa = \Sigma_p \Sigma_q C_{ph} \cdot v_g^2 \cdot \tau$, where p and q denote the phonon branch and wave vector, respectively, C_{ph}, v_g, τ is the specific heat capacity, group velocity and relaxation time of a specific phonon mode [35]. In Fig. 4, we can see that some phonons belonging to the high frequency part in the low frequency island ($1 \sim$ 5THz) have relatively short lifetime, which is also mentioned in the previous work [10]. Combining the data shown in Fig. 4(a, b), we can conclude that, although the phonon lifetime of the modes in the middle and high frequency islands is comparable with that in the low frequency island, their contribution to κ can be simply ignored, due to the almost zero group velocity. Meanwhile, because the phonon distribution obeys the Bose-Einstein statistics, the phonons of middle and high frequency islands are hardly thermally occupied at room temperature. The

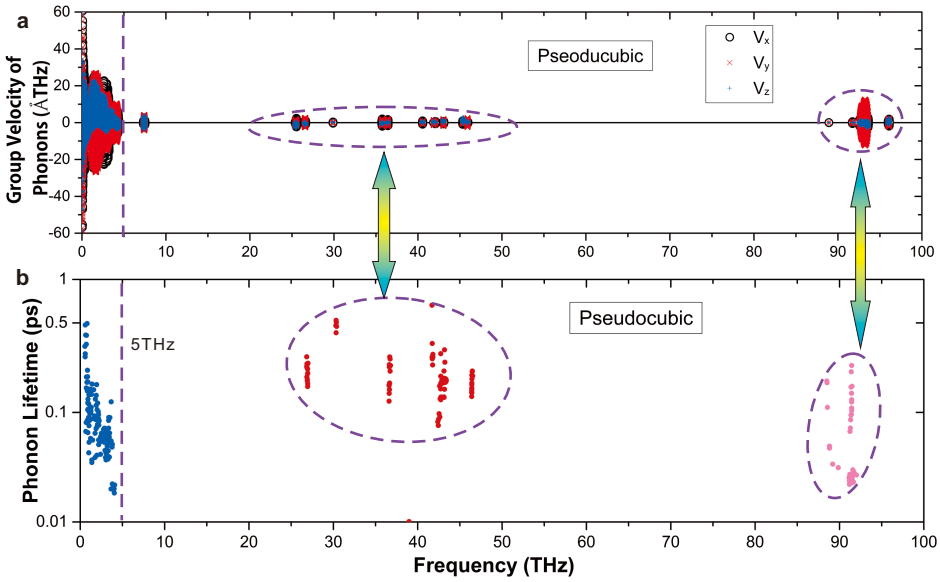

FIG. 4: The frequency dependent (a) phonon group velocities and (b) phonon lifetime of pseudocubic phase MAPI. In (b), the blue, red and pink data points correspond to the low, middle and high frequency islands, respectively, which are shown in the right panel of Fig. 3(a).

plot of Bose-Einstein occupation function with respect to frequency at 300 K can be found in Supplemental Material. This reason along with the very small group velocities (phonon modes are strongly localized) rules out the contributions to κ from phonons belonging to the middle and high frequency islands. Therefore, the κ of MAPI mainly stems from the phonon modes in the low frequency island, which is directly associated with the vibrational modes of inorganic cages and the coupling between the cage and the whole organic cluster.

C. VDOS and deformation charge density of MAPI

In order to further elucidate the coupling between the organic and inorganic components, we calculate the VDOS of PbI_3^- cages with and without the MA^+ cluster. All the partial VDOS results are obtained from EAIMD. From Fig. 5, we can clearly see that, for the case without MA^+, the VDOS of Pb and I ions are almost the same. This implies that the Pb and I ions have synergistic vibration in the PbI_3^- octahedra. In contrast, for the case with the organic cluster, we see that the VDOS of I ions are higher than that of Pb ions for the frequency range $>$ 4 THz, exhibiting evident split of vibrations between Pb and I ions. This proves that the presence of the organic cluster influences the vibrations of I ions much more than that of Pb ions, and such influence can even extend to the frequency range higher than 7 THz (the long tail of VDOS of I ions). To provide a direct explanation, in the inset of Fig. 5 we present the deformation charge density of MAPI to show the charge transfer in MAPI during the process of chemical bonding formation.

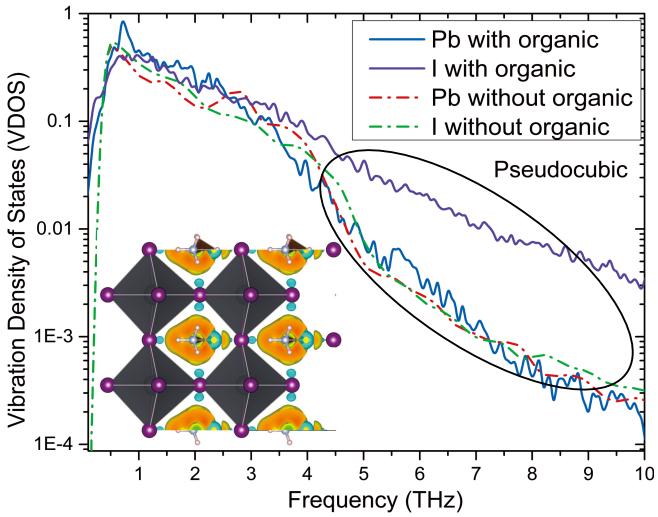

FIG. 5: Comparison of the partial vibrational density of states of Pb and I ions in the inorganic cages with and without MA^+ cluster. The solid lines are the results of normal pseudocubic MAPI structure (with MA^+) and the dash-dotted lines represent the empty pseudocubic inorganic cages (without MA^+). (Inset) The deformation charge density of pseudocubic MAPI with isosurface value 0.005. The green and yellow colors represent the negative and positive charge densities, respectively.

The deformation charge density was calculated by the difference between the real charge densities after chemical bonding formation and the original charge densities of atoms on sites. From the deformation charge density, we see that, the organic cluster possesses positive charge and only the I ions provide the negative charge environment

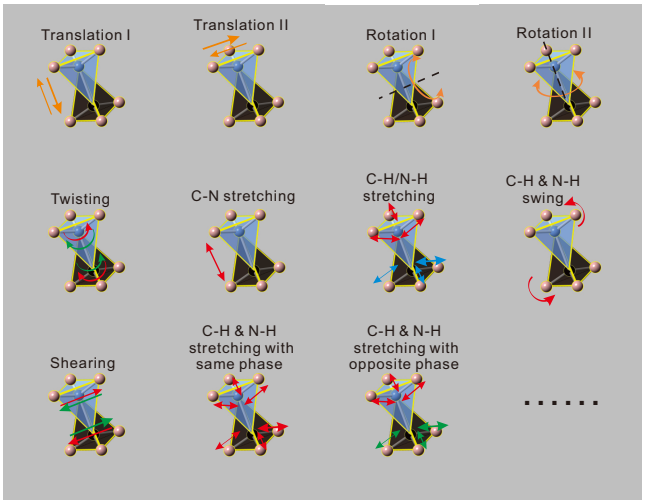

FIG. 6: Schematic of some representative phonon modes associated with the MA^+ cluster in the pseudocubic phase perovskite solar cell. The arrows indicate the movement of the entire cluster or atoms. For brevity, only the MA^+ cluster is shown.

around the MA^+. This means that the MA^+ cluster interacts directly with the I ions, and then influences the PbI_3^+ cages indirectly. This can be understood considering the fact that the Pb ions reside in the center of the octahedra and the $MA^+ - Pb$ interactions are shielded by the I ions. This is the direct reason for the split VDOS observed in Fig. 5.

D. Direct observation of individual phonon modes and quantification of phonon anharmonicity in MAPI

To directly observe the atomic motions of all phonon modes in MAPI, with the help of normal mode analysis we find out the total 36 phonon modes of the pseudocubic MAPI (the unit cell contains 12 basis atoms). We present all these modes in the supporting movies (Vibrational modes $01-36$) with label in the sequence of frequency from low to high. Among these motions, we can easily distinguish the modes that belong to or are dominated by the MA^+ cluster. Some representative modes associated with MA^+ are schematically shown in Fig. 6. From the supporting movies (Vibrational modes $01-12$) we can see that only the collective motions of the entire MA^+ cluster can drive a relatively large vibration of the inorganic cages, meaning effective coupling between the two components. We also found that, all such coupled modes indeed occurs at low frequencies, which belongs to the lowest frequency island as shown in the right panel of Fig. 3(a). Again, it proves that the strong coupling between the organic cluster and the inorganic cages only happens in the low frequency range ($<$ 7 THz).

To quantitatively characterize the effects of the collective motions of the rotational and translational modes and analyse the anharmonicity of these phonon modes, in Fig. 7 we present the potential energy change when the MA^+ cluster is displaced with a certain rotational angle or a translational displacement, corresponding to the rotation I/II and translation I/II modes as illustrated in Fig. 6. The magnitude of both the rotational angle and the translational displacement are extracted from the real EAIMD simulations, the same data used for the above SED calculation. Every configuration that is used to calculate Fig. 7 is taken from the real vibrational structure of EAIMD simulation. Theoretically, these configurations mean that the rest positions are fully relaxed, but the lattice shape and volume are fixed during this process. To quantify the anharmonic effect of each mode, we also perform quadratic fitting of the potential energy at the equilibrium position. The detailed information are listed in Table. I. It is interesting to observe that, for both rotational and translational modes of MA^+, the oscillating amplitude is not exactly symmetric with respect to the equilibrium position, in particular for the rotational modes. This phenomenon can also be observed in the supporting movies(Rotation I). Meanwhile, we note that the potential energy curves for the two translational modes are perfectly quadratic, corresponding to pure harmonic oscillations. However, for the two rotational modes the potential energy curves largely deviate from the quadratic fitting, showing strong phonon anharmonicity. This result reveals that the translational motions of MA^+ should have little scattering with phonons of the inorganic lattice and the anharmonic effects due to the motion of the MA^+ cluster mainly originate from its rotational movement. Considering that the low frequency phonons associated with the MA^+ cluster mainly reside in the range of $1 \sim 5$THz as shown in the PDOS (the right panel of Fig. 3(a)) and their corresponding phonon lifetime is relatively short (Fig. 4(b)), we conclude that the strong scattering between the rotational modes of the MA^+ cluster and other low frequency phonons belonging to the inorganic cage drive the ultra-low κ of the hybrid organic-inorganic MAPI. This is the fundamental mechanism why the perovskite solar cell possesses such low lattice thermal conductivity.

In Table. I, we calculate the oscillating energy of these modes defined as $\Delta E = E_{max} - E_{min}$, where E_{min} is the minimum potential energy corresponding to the equilibrium position of respective oscillation and E_{max} is possible highest potential energy during the oscillation (shown in Fig. 7). We can clearly see that the ΔE of both rotational modes are much higher than that for the two translational modes. This provides further evidence to prove that the rotational modes dominate the interactions or coupling between the MA^+ cluster and the inorganic lattice. This result is consistent with the previous experimental observation [8].

Before closing, it is worth noting an interesting phenomenon in Fig. 7(a), where the potential energy of the system does not increase monotonically when the MA^+

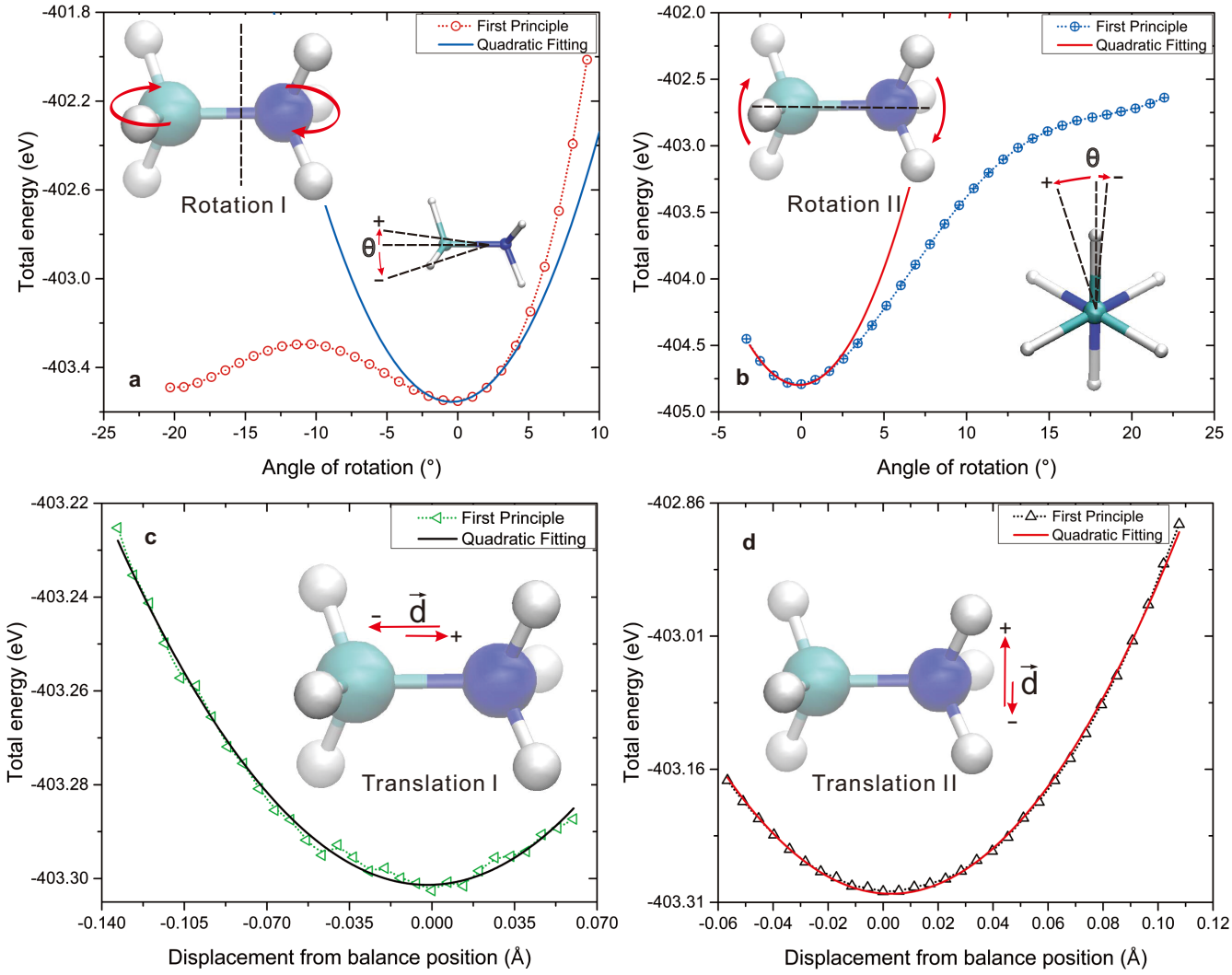

FIG. 7: Analysis of phonon anharmonicity of representative rotational and translational modes in the pseudocubic phase perovskite solar cell by first-principles calculations (supercell $2 \times 2 \times 2$). (a, b) represents the change of the potential energy of the system with respect to the rotational angle for the modes of rotation I and II, respectively. (c, d) illustrates the corresponding results for the modes of translation I and II, respectively. The solid lines are quadratic fitting to the energy change. (Insets) Schematic of the movement of the MA^+ cluster.

TABLE I: The values of potential energy change for rotational and translational modes of MA^+ shown in Fig. 7.

Type of modes	Farthest negative amplitude	Farthest positive amplitude	Minimum potential energy (E_{min})	Maximum potential energy (E_{max})	Oscillating energy ($\Delta E = E_{max} - E_{min}$)
Rotation I	$-20.31°$	$9.13°$	-403.5515 eV	-402.0132 eV	1.5383 eV
Rotation II	$-3.32°$	$21.97°$	-404.7913 eV	-402.6384 eV	2.1529 eV
Translation I	-0.133 Å	0.060 Å	-403.3026 eV	-403.2253 eV	0.0773 eV
Translation II	-0.0566 Å	0.108 Å	-403.2979 eV	-402.8839 eV	0.4140 eV

cluster rotates in a negative angle. Instead, there exists a meta-stable potential energy valley with rotation angle of around $-20°$. This small potential energy valley induces an additional oscillation during the journey of the MA^+ cluster going back to the global minima. This phenomenon can be observed straightforwardly in the corresponding mode from the supporting movie (Rotation I). From the movie, we observe that when MA^+ move to the negative amplitude position, the C − H bond length tends to extend. This is the reason behind the

meta-stable potential energy valley in Fig. 7(a). From the supporting movies (Vibrational modes $25-36$) we can also see the inner motions of the MA^+ cluster, as we mentioned above, such as the shearing and stretching of the $C-N$ bonds, the swing and stretching of the $C-H$ and $N-H$ bonds. We also confirm that, the phonon modes associated with the $C-N$ bonds correspond to the middle frequency island and the modes associated with the $C-H$ and $N-H$ bonds belong to the high frequency island. All of these results are consistent with the PDOS (right panel of Fig. 3(a)) and provide additional proof for our previous conclusion, based on the dynamics of the system at finite temperature.

IV. SUMMARY

To summarize, through direct non-equilibrium *ab initio* molecular dynamics simulation we study the thermal transport property of the hybrid organic-inorganic halide perovskite ($CH_3NH_3PbI_3$) solar cells in pseudocubic and tetragonal phases. We analyze the phonon dispersion curves of the MAPI structures based on first-principles calculations. The phonon modes in MAPI are found to split into three major islands with huge energy gap between the neighbouring islands, which naturally prevent the cross-island phonon scattering. However, this does not intuitively result in high thermal conductivity. On the contrary, we identify the MAPI possesses ultra-low lattice thermal conductivity for both phases, which is well consistent with the previous theoretical and experimental studies. With the aid of phonon group velocity, phonon lifetime and normal mode analysis, we provide a thorough explanation to the fundamental mechanism underlying the ultra-low thermal conductivity: the overall thermal transport in MAPI are dominated by the intrinsic phonons of the inorganic cages in the low frequency island ($<$ 7 THz) with negative contribution from the interaction or coupling between the rotational motion of the inorganic cluster and the organic cage in the same frequency range. In contrast, the phonon modes in the middle and high frequency islands, which are associated with the internal motions of the organic cluster alone, have negligible contribution to the overall heat transport in MAPI, primarily due to the strong localization (nearly zero group velocity) and low thermal occupation at room temperature of such modes. Our study highlights the physical origin of the ultralow thermal conductivity of the hybrid organic-inorganic halide perovskite structures, and also provides new insights into the phonon transport from the view of organic-inorganic coupling (rotational vs. translational), which would be of great significance to the design and discovery of novel perovskite materials for better energy conversion performance. The method of freezing partial freedoms of the organic cluster to avoid the imaginary phonon modes can also be straightforwardly applied to broad ordered-disordered materials, such as metal-organic frameworks, guest atoms in clathrates, and phonon liquid thermoelectrics.

Acknowledgement

S.Y.Y. appreciates Dr. Stephen Stackhouse (University of Leeds) for providing the modified VASP code. The authors gratefully acknowledge the computing time granted by the John von Neumann Institute for Computing (NIC) and provided on the supercomputer JURECA at Jülich Supercomputing Centre (JSC) (Project ID: JHPC25). The SED simulations were performed with computing resources granted by the Jülich Aachen Research Alliance-High Performance Computing (JARA-HPC) from RWTH Aachen University under project No. jara0135.

[1] M. Liu, M. B. Johnston, and H. J. Snaith, Nature **501**, 395 (2013).
[2] H. J. Snaith, J. Phys. Chem. Lett. **4**, 3623 (2013).
[3] A. Kojima, K. Teshima, Y. Shirai, and T. Miyasaka, J. Am. Chem. Soc. **131**, 6050 (2009).
[4] M. M. Lee, J. Teuscher, T. Miyasaka, T. N. Murakami, and H. J. Snaith, Science **338**, 643 (2012).
[5] D. Shi, V. Adinolfi, R. Comin, M. Yuan, E. Alarousu, A. Buin, Y. Chen, S. Hoogland, A. Rothenberger, K. Katsiev, et al., Science **347**, 519 (2015).
[6] S. D. Stranks, G. E. Eperon, G. Grancini, C. Menelaou, M. J. P. Alcocer, T. Leijtens, L. M. Herz, A. Petrozza, and H. J. Snaith, Science **342**, 341 (2013).
[7] J. Burschka, N. Pellet, S.-J. Moon, R. Humphry-Baker, P. Gao, M. K. Nazeeruddin, and M. Grätzel, Nature **499**, 316 (2013).
[8] A. Pisoni, J. Jaimovi, O. S. Barii, M. Spina, R. Gal, L. Forr, and E. Horvth, J. Phys. Chem. Lett. **5**, 2488 (2014).
[9] T. Hata, G. Giorgi, and K. Yamashita, Nano Lett. **16**, 2749 (2016).
[10] X. Qian, X. Gu, and R. Yang, Appl. Phys. Lett. **108** (2016).
[11] Y. He and G. Galli, Chem. Mater. **26**, 5394 (2014).
[12] A. M. A. Leguy, J. M. Frost, A. P. McMahon, V. G. Sakai, W. Kockelmann, C. Law, X. Li, F. Foglia, A. Walsh, B. C. ORegan, et al., Nat. Commun. **6** (2015).
[13] C. Quarti, G. Grancini, E. Mosconi, P. Bruno, J. M. Ball, M. M. Lee, H. J. Snaith, A. Petrozza, and F. D. Angelis, J. Phys. Chem. Lett. **5**, 279 (2014).
[14] C. Quarti, E. Mosconi, and F. De Angelis, Phys. Chem. Chem. Phys. **17**, 9394 (2015).
[15] F. Brivio, J. M. Frost, J. M. Skelton, A. J. Jackson, O. J. Weber, M. T. Weller, A. R. Goñi, A. M. A. Leguy, P. R. F. Barnes, and A. Walsh, Phys. Rev. B **92**, 144308 (2015).

[16] S. Stackhouse, L. Stixrude, and B. B. Karki, Phys. Rev. Lett. **104**, 208501 (2010).
[17] H. Kim, M. H. Kim, and M. Kaviany, J. Appl. Phys. **115** (2014).
[18] G. Kresse and J. Furthmüller, Phys. Rev. B **54**, 11169 (1996).
[19] G. Kresse and J. Furthmüller, Comp. Mater. Sci. **6**, 15 (1996), ISSN 0927-0256.
[20] F. Müller-Plathe, J. Chem. Phys. **106**, 6082 (1997).
[21] E. Mosconi, C. Quarti, T. Ivanovska, G. Ruani, and F. De Angelis, Phys. Chem. Chem. Phys. **16**, 16137 (2014).
[22] C. Motta, F. El-Mellouhi, S. Kais, N. Tabet, F. Alharbi, and S. Sanvito, Nat. Commun. **6** (2015).
[23] A. Togo and I. Tanaka, Scr. Mater. **108**, 1 (2015).
[24] J. P. Perdew, K. Burke, and M. Ernzerhof, Phys. Rev. Lett. **77**, 3865 (1996).
[25] P. E. Blöchl, Phys. Rev. B **50**, 17953 (1994).
[26] G. Kresse and D. Joubert, Phys. Rev. B **59**, 1758 (1999).
[27] A. Tkatchenko and M. Scheffler, Phys. Rev. Lett. **102**, 073005 (2009).
[28] J. M. DICKEY and A. PASKIN, Phys. Rev. **188**, 1407 (1969).
[29] X. Zhang and J. Jiang, J. Phys. Chem. C **117**, 18441 (2013).
[30] J. A. Thomas, J. E. Turney, R. M. Iutzi, C. H. Amon, and A. J. H. McGaughey, Phys. Rev. B **81**, 081411 (2010).
[31] J. M. Larkin, J. E. Turney, A. D. Massicotte, C. H. Amon, and A. J. H. McGaughey, J. Comput. Theor. Nanosci. **11**, 249 (2014).
[32] X. Zhang, H. Bao, and M. Hu, Nanoscale **7**, 6014 (2015).
[33] M. T. Dove, *Introduction to Lattice Dynamics* (Cambridge University Press, Cambridge, 1993).
[34] M. Bokdam, T. Sander, A. Stroppa, S. Picozzi, D. D. Sarma, C. Franchini, and G. Kresse, Scientific Reports **6**, 28618 (2016).
[35] S.-Y. Yue, T. Ouyang, and M. Hu, Sci. Rep. **5**, 15440 (2015).